Visualization of O-O peroxo-like dimers in high-capacity layered oxides for Li-ion batteries

Eric Mccalla, Artem M Abakumov, Matthieu Saubanère, Dominique Foix, Erik J Berg, Gwenaelle Rousse, Marie-Liesse Doublet, Danielle Gonbeau, Petr Novak, Gustaaf van Tendeloo, et al.

To cite this version:

Eric Mccalla, Artem M Abakumov, Matthieu Saubanère, Dominique Foix, Erik J Berg, et al.. Visualization of O-O peroxo-like dimers in high-capacity layered oxides for Li-ion batteries. Science, 2015, 305 (6267), pp.1516-1521. 10.1126/science.aac8260 . hal-01253767

Visualization of O-O peroxo-like dimers in high-capacity layered oxides for Li-ion batteries

Eric McCalla,[1,2,3,4] Artem M. Abakumov,[5,6] Matthieu Saubanère,[2,3,7]
Dominique Foix,[2,3,8] Erik J. Berg,[9] Gwenaelle Rousse,[1,3,10] Marie-Liesse Doublet,[2,3,7]
Danielle Gonbeau,[2,3,8] Petr Novák,[9] Gustaaf Van Tendeloo,[5]
Robert Dominko,[4] Jean-Marie Tarascon[1,2,3,10]*

Lithium-ion (Li-ion) batteries that rely on cationic redox reactions are the primary energy source for portable electronics. One pathway toward greater energy density is through the use of Li-rich layered oxides. The capacity of this class of materials (>270 milliampere hours per gram) has been shown to be nested in anionic redox reactions, which are thought to form peroxo-like species. However, the oxygen-oxygen (O-O) bonding pattern has not been observed in previous studies, nor has there been a satisfactory explanation for the irreversible changes that occur during first delithiation. By using Li_2IrO_3 as a model compound, we visualize the O-O dimers via transmission electron microscopy and neutron diffraction. Our findings establish the fundamental relation between the anionic redox process and the evolution of the O-O bonding in layered oxides.

Because lithium-ion (Li-ion) batteries have the highest energy density of all commer-cially available batteries, they are able to power most consumer electronics and have emerged as the technology of choice for powering electric vehicles. Li-ion batteries may also be used for grid storage and load-leveling for renewable energy. Current state-of-the-art positive electrodes use layered rock salt oxides ($LiCoO_2$ and its derivatives), spinel ($LiMn_2O_4$), or polyanionic compounds such as olivine-type $LiFePO_4$ (*1*). One push to increase the practical capacity limit of $LiCoO_2$ is via chemical substitution aimed at stabilizing the layered framework. The partial replacement of Co^{3+} with Ni^{2+} and Mn^{4+} has led to the $Li(Ni_xMn_yCo_{1-x-y})O_2$ layered oxides being coined as stoichiometric nickel manganese cobalt (NMC) oxides. These compounds have improved safety and capacities approaching 200 mA·hour/g. Further substitution of the transition metals by Li results in capacities exceeding 270 mA·hour/g. These materials are referred to as Li-rich layered oxides, as some Li ions now occupy crystallographic sites in the transition metal layers in the ordered rock salt structure (*2*, *3*). During the first charge, these compounds undergo a transformation such that subsequent charge-discharge curves take an S shape without clear redox plateaus (as seen for $Li_2Ir_{0.75}Sn_{0.25}O_3$ in Fig. 1C). Partial oxidation of the oxygen sublattice upon Li removal, leading to an increased capacity, has been conjectured (*4*–*12*). The high capacity is rooted in the cumulative reversibility of both cationic and anionic redox processes ($2O^{2-} \rightarrow O_2^{n-}$, where n = 1, 2, or 3) (*13*–*15*). We speculated, but did not observe, that this oxidation of oxygen results in the formation of peroxo-like species with shortened O-O distances. Nevertheless, such studies demonstrate that the Li-(de)intercalation chemistry does not rely solely on cationic redox reactions as the source of energy storage; the oxygen sublattice is active as well.

Such O-O pairing in the oxygen lattice, resulting from the formation of O_2^{n-} species, predominantly occurs in compounds that have highly covalent metal-oxygen bonding—that is, systems showing a high degree of M(d)-O(sp) band overlap (*13*–*16*). Although this description of the oxidation of the oxygen sublattice is relatively new, the activity of the anionic network for chalcogenide (Ch)–based electrodes has long been recognized (*17*). By properly selecting cation-anion pairs, Rouxel showed the feasibility of tuning the degree of the metal M(3d)-Ch(sp) band mixing so as to trigger the formation of S-S dimers or Te-Te-Te trimers, as observed for iridium tellurides (*17*). Moreover, by performing a survey of various compounds such as $Li_2Ru_{1-x}Sn_xO_3$ (*13*), $Li_{4.27}Fe_{0.56}TeO_6$ (*16*), Li_4NiTeO_6 (*18*), and Li_4FeSbO_6 (*19*), we have demonstrated that the stability of the oxygen close-packed framework against O_2 evolution at high potential is highly tunable with composition. This finding is particularly important because this process leads to large irreversible capacities and poor long-term cycling (*16*, *19*, *20*). Layered compounds containing 4d metals have recently been shown to have reversible capacities of 300 mA·hour/g that involve a reversible anionic redox process (*21*). There is no direct structural evidence for the presence of peroxo-like species in any layered oxide, nor is it clear to what extent oxygen can be reversibly oxidized (i.e., the value of n in O_2^{n-} remains an enigma).

We address these questions via a model system consisting of a Li-rich layered phase with Ir as a 5d metal so as to increase the covalency and minimize the unwanted cationic migration during charge-discharge cycling with the larger Ir atoms. $Li_2Ir_{1-x}Sn_xO_3$ compounds with x = 0, 0.25, and 0.5 were prepared as described in the supplementary materials (*22*). Figure 1A (left) shows the structure of pristine Li_2IrO_3, which displays the cubic close-packed O3 stacking of the Li layers and the $Li_{1/3}Ir_{2/3}O_2$ slabs, where each Li cation is surrounded by six Ir cations to form a honeycomb-like ordering pattern. Figure 1B and fig. S1 show x-ray powder diffraction (XRD) patterns of the pristine $Li_2Ir_{1-x}Sn_xO_3$ materials and demonstrate typical shifts in peak positions consistent with a solid solution, confirmed by the progression of lattice parameters seen in table S1. Figure 1, C and D, and fig. S2 show the electrochemical performance of the x = 0, 0.25, and 0.5 materials. The x = 0.25 and 0.5 samples show cycling behavior typical of Li-rich oxides: two plateaus on first charge in the graphs of voltage versus y in $Li_yIr_{1-x}Sn_xO_3$, with a transformation taking place such that the second charge cycle is markedly different from the first, with an S shape now visible.

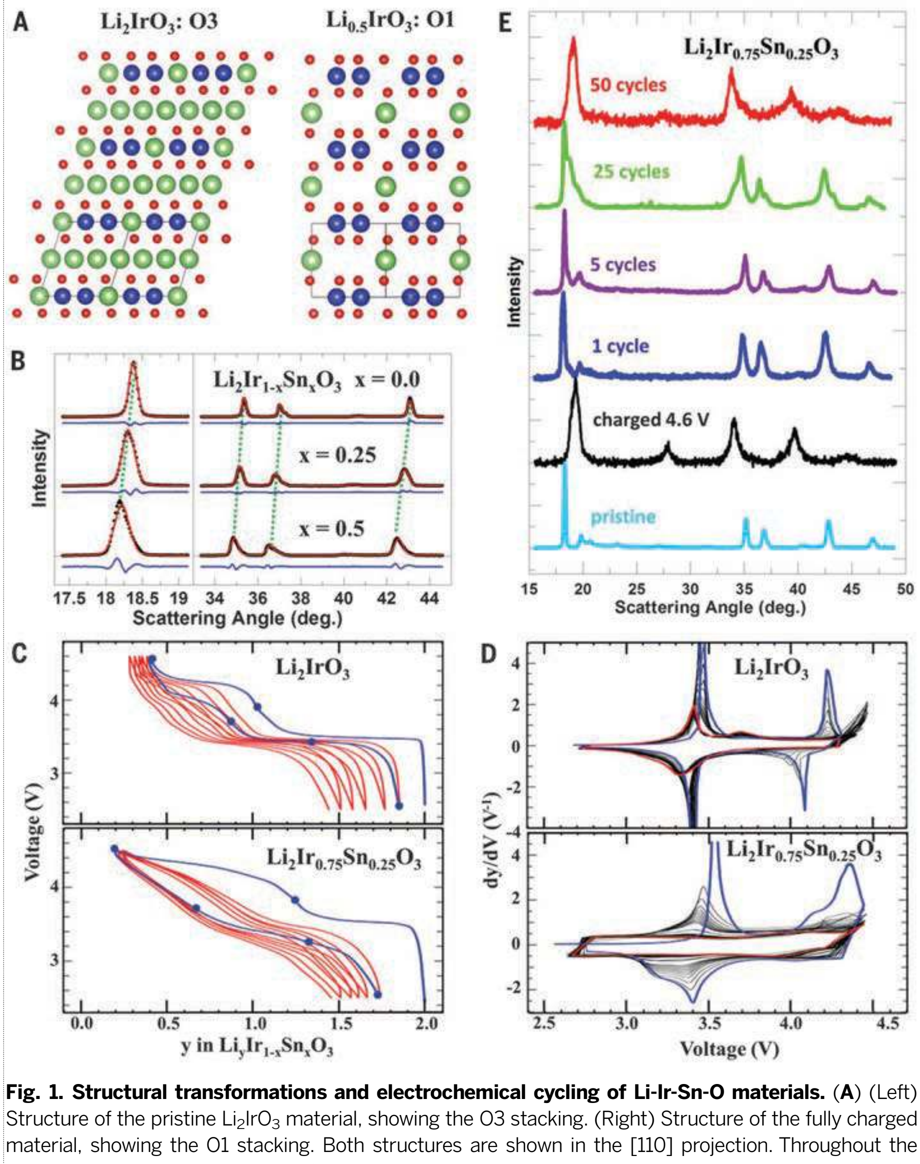

Fig. 1. Structural transformations and electrochemical cycling of Li-Ir-Sn-O materials. (**A**) (Left) Structure of the pristine Li_2IrO_3 material, showing the O3 stacking. (Right) Structure of the fully charged material, showing the O1 stacking. Both structures are shown in the [110] projection. Throughout the figures Ir is blue, Li is green, and O is red. (**B**) XRD patterns for the pristine materials with varying Sn content, fitted by taking stacking faults into account with the FAULTS software. Green dashed lines show peak shifts, consistent with an increase in cell volume as Sn content increases. Complete patterns are included in fig. S1. (**C**) Voltage curves showing the first 10 cycles at C/10 between 2.5 and 4.6 V. The first cycle shown in blue, and blue circles represent specific compositions, as referred to in Fig. 2D. (**D**) Derivative curve showing the evolution of the redox peaks between the first (blue) and 50th (red) cycles. (**E**) XRD patterns for $Li_2Ir_{0.75}Sn_{0.25}O_3$ after various electrochemical tests, showing a gradual conversion during extended cycling until the final scan looks similar to that of the first charged sample.

---

[1]Collège de France, Chimie du Solide et de l'Energie, FRE 3677, 11 Place Marcelin Berthelot, 75231 Paris Cedex 05, France. [2]ALISTORE–European Research Institute, FR CNRS 3104, 80039 Amiens, France. [3]Réseau sur le Stockage Electrochimique de l'Energie (RS2E), FR CNRS 3459, France. [4]National Institute of Chemistry, Hajdrihova 19, SI-1000 Ljubljana, Slovenia. [5]Electron Microscopy for Materials Science (EMAT), University of Antwerp, Groenenborgerlaan 171, B-2020, Antwerp, Belgium. [6]Center for Electrochemical Energy Storage, Skolkovo Institute of Science and Technology, 3 Nobel Street, 143026 Moscow, Russia. [7]Institut Charles Gerhardt, CNRS UMR 5253, Université Montpellier, Place Eugène Bataillon, 34 095 Montpellier, France. [8]IPREM/ECP (UMR 5254), University of Pau, 2 Avenue Pierre Angot, 64053 Pau Cedex 9, France. [9]Electrochemistry Laboratory, Paul Scherrer Institut, CH-5232 Villigen PSI, Switzerland. [10]Sorbonne Universités–UPMC Univ Paris 06, 4 Place Jussieu, F-75005 Paris, France.
***Corresponding author. E-mail: jean-marie.tarascon@college-de-france.fr**

This transformation indicates the presence of either a solid solution during the removal of lithium or a broad energy distribution of the lithium sites. By contrast, the Li_2IrO_3 sample shows that the plateaus seen on first charge are far more robust, as reported by Kobayashi *et al.* (*23*). However, the *dy/dV* curves show a steady decrease in the size of the redox peaks with extended cycling, yielding a substantial capacity fade for both samples; the $x = 0$ composition in particular shows none of the voltage fade seen in many Li-rich oxides (*3*, *14*).

Because the $x = 0$ and 0.25 samples behave differently, the structural evolution was studied in detail for both systems. Figure 1E shows the associated changes in the XRD patterns for the $x = 0.25$ sample during extended cycling. At the end of charge, the XRD pattern indexes to that of an O1-type structure with a hexagonal close-packed stacking (right image in Fig. 1A). After the first cycle, the XRD pattern returns primarily to that of the pristine O3 structure, though with the appearance of a few small new peaks. These peaks grow with extended cycling until only they remain after 50 cycles, and the peaks attributed to the O3 structure are no longer present. This same process occurs in Li_2IrO_3 samples (fig. S3).

Figure 2 covers the redox processes that occur during electrochemical cycling. The x-ray photoelectron spectroscopy (XPS) results shown in Fig. 2, A and B, and fig. S4 are consistent with previous results for Ru-based systems (*13*–*15*) wherein both metal and oxygen oxidations take place during charge. Here, Ir begins in the 4+ state and is oxidized during the first plateau, which ends at 3.9 V. This represents the greatest positive shift in the Ir 4f peak, and it is tempting to attribute this shift to Ir^{5+}, based on the fact that nearly 1 Li atom is removed from Li_2IrO_3 ($x = 0$) and 0.75 is removed from $Li_2Ir_{0.75}Sn_{0.25}O_3$ ($x = 0.25$), as shown in Fig. 1C. However, unlike in Ru-based systems, we can already detect the presence of peroxo-like species in the O 1s peaks in the XPS spectra at mid-charge, as shown in Fig. 2A ($x = 0$) and fig. S4 ($x = 0.25$). This suggests a mixed redox process, such that Ir is not strictly in the 5+ state but instead the electron being removed during charge is taken from both Ir and O, which is expected given the highly covalent Ir-O bond. Figure 2C shows the progression of the fraction of oxygen in the peroxo-like species during cycling for both samples. In each case, the fully charged state contains nearly half of the sample's oxygen in the peroxo-like species O_2^{n-}. Upon discharge, the peroxo-like species is reduced back to O^{2-} between 3.7 and 2.5 V for both samples, though it occurs slightly earlier in discharge for the Sn-containing material where the peroxo-like species is reduced by the time a lithium content of 1.33 atoms is reached. This difference suggests that Sn promotes the reversibility of the anionic redox process over a wider potential window (3.7 to 3.25 V) with less hysteresis. This change may be attributed to added flexibility in the oxygen network due to the presence of Sn, as previously proposed (*13*). The Li_2IrO_3 sample is therefore a Li-rich oxide, where the peroxo-like species are seen by XPS without immediate conversion to an S curve in the cycling data. We therefore have the opportunity to study anionic redox and the conversion to S curve independently and to establish the true cause of the transformations seen in other Li-rich oxides. Figure 2D shows the change in Bader charge calculated with density functional theory (DFT) as Li is removed from Li_2IrO_3. This also shows mixed redox throughout the Li extraction, in agreement with the XPS results.

These results imply that the local distortions in the oxygen lattice associated with the formation of peroxo-like species can be observed directly by transmission electron microscopy (TEM). The reason such information is available for the Li_2IrO_3 system is that the charged sample takes an O1 structure (Fig. 1A, refinements shown in fig. S5, and structure given in table S2) such that the projection of the oxygen columns becomes available along the *c* axis without overlapping with the columns of Ir or Li. The [010], [100], and [001] high-angle annular dark-field scanning transmission electron microscopy (HAADF-STEM) images of the charged $Li_{0.5}IrO_3$ sample show the highly ordered O1 structure viewed across (Fig. 3A and fig. S6, left) and along (Fig. 3B and fig. S6, right) the *c* axis. These images demonstrate perfect honeycomb ordering of the Ir cations on the transition metal layer and very little migration of Ir to the now nearly empty Li layer. This highly ordered structure is very unusual for this class of Li-rich layered oxides and allows for visualization of the oxygen columns using annular bright field STEM (ABF-STEM) imaging (Fig. 3, B and C, and fig. S7). The ABF-STEM technique has been proven to accurately reveal the positions of "light" elements (such as Li, O, and even H) in the presence of atomic entities with much higher scattering power (*24*–*27*). The correspondence between the experimental [001] HAADF- and ABF-STEM images and the crystal structure projection was established with the help of the simulated

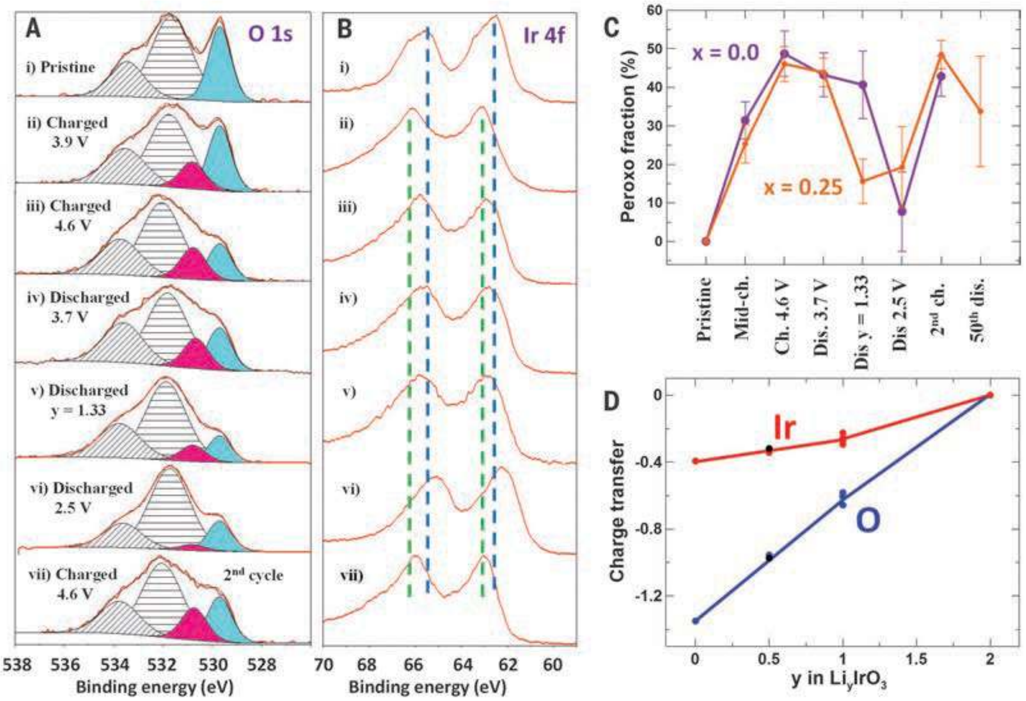

Fig. 2. Changes in cationic and anionic oxidation states during Li_2IrO_3 cycling. (**A**) Oxygen 1s core XPS peaks at various points after electrochemical cycling. The O^{2-} (blue) and O_2^{n-} (red) peaks are attributed to the sample, whereas the two gray striped peaks represent the surface species and electrolyte decomposition products, as described in (*13*). (**B**) Iridium 4f core XPS peaks. The dashed lines are guides for the eye indicating the position of the pristine (4+) peaks (blue) and the highest oxidation state (5+) (green). (**C**) Fraction of lattice oxygen attributed to peroxo for $Li_yIr_{1-x}Sn_xO_3$ samples. The samples discharged to $y = 1.33$ were stopped at 3.4 V for Li_2IrO_3 and 3.25 V for $Li_2Ir_{0.75}Sn_{0.25}O_3$, as shown in Fig. 1C. (**D**) Results for change in Bader charge with respect to the pristine sample obtained from DFT calculations. These are consistent with the XPS results showing mixed redox throughout the charge process. All calculations were performed on the O3 structure, except for the black points at $y = 0.5$, which were obtained for the O1 structure. The red and blue lines are guides for the eye and illustrate continuous mixed redox during charge.

images, using the crystallographic data in table S2 (fig. S8). The projected symmetry of the IrO$_6$ octahedra is expected to be close to sixfold symmetry, corresponding to all nearly equal O-O separations. However, the shape of these octahedra in the experimental [001] ABF-STEM image is clearly driven toward threefold symmetry due to the formation of shortened (black dumbbells) and lengthened (left blank) projected O-O separations (Fig. 3C). The distinct difference in the short and long O-O projected separations is evident from a comparison of the corresponding ABF intensity profiles (Fig. 3D). The values of the projected O-O separations were estimated from the analysis of a histogram of their distribution (fig. S11), which demonstrates peaks centered at 1.56 and 1.83 Å, reflecting the average values of the shortened and lengthened projected O-O distances (Table 1).

The observed distortion of the oxygen sublattice is in line with the atomic arrangement obtained from ab initio calculations. Figure 3E shows the [001] projection, as obtained on the basis of DFT calculations for the charged Li$_{0.5}$IrO$_3$ sample. This calculation shows shortened projected O-O distances for pairs of oxygen atoms (joined by red lines) lying between two Ir atoms. Figure 3E also shows the Fukui function, which probes the change in the electron density as a result of an infinitesimal change in the total number of electrons. The Fukui function can be used to probe the redox-active center (atomic and/or molecular entities affected by the charge variation; i.e., where the electronic charge is varying) in an electrochemical reaction. Here, the Fukui function shows changes in electron density around both Ir and O. The shape of the Fukui function around the oxygen atom shows overlapping lobes along the axis joining the O-O pairs with short separations, consistent with the expectation of partially empty antibonding σ* orbitals if peroxo-like species are formed. By contrast, fig. S9 shows no such orbital overlap in the pristine material.

The distortion pattern observed on a local scale was confirmed using the structural refinements of the bulk structure from neutron powder diffraction (NPD) data for the pristine and fully charged Li-Ir-O samples (included in figs. S5 and S10). The [001] projections of the refined structures are shown overlaid in Fig. 3F (for this image, the unit cell of the pristine structure was shrunk slightly to overlap but the aspect ratio was not changed). This shows the displacement in the oxygen lattice taking place during the formation of the peroxo-like species and is consistent with the ABF-STEM image. This also serves to show that changes seen in projected distance with ABF-STEM do in fact correspond to actual atomic displacements.

Table 1 presents a summary of the O-O distances determined with different methods, all confirming a distortion in the lattice such that oxygen atoms approach each other to form O-O pairs lying between two adjacent Ir atoms. By contrast, no such distortions have been seen for materials that do not involve anionic redox [e.g., the stoichiometric NMC compounds given in Table 1 with values based on neutron diffraction (*28*)]. However, the O-O distances measured here do not approach the ~1.5 Å O-O distances seen for peroxide species in highly ionic compounds, such as Li$_2$O$_2$, or in systems where oxygen pairs lie in cavities within the cationic network, as seen in a few perovskite materials (*29*). In more covalent systems, such as those discussed here, the formation

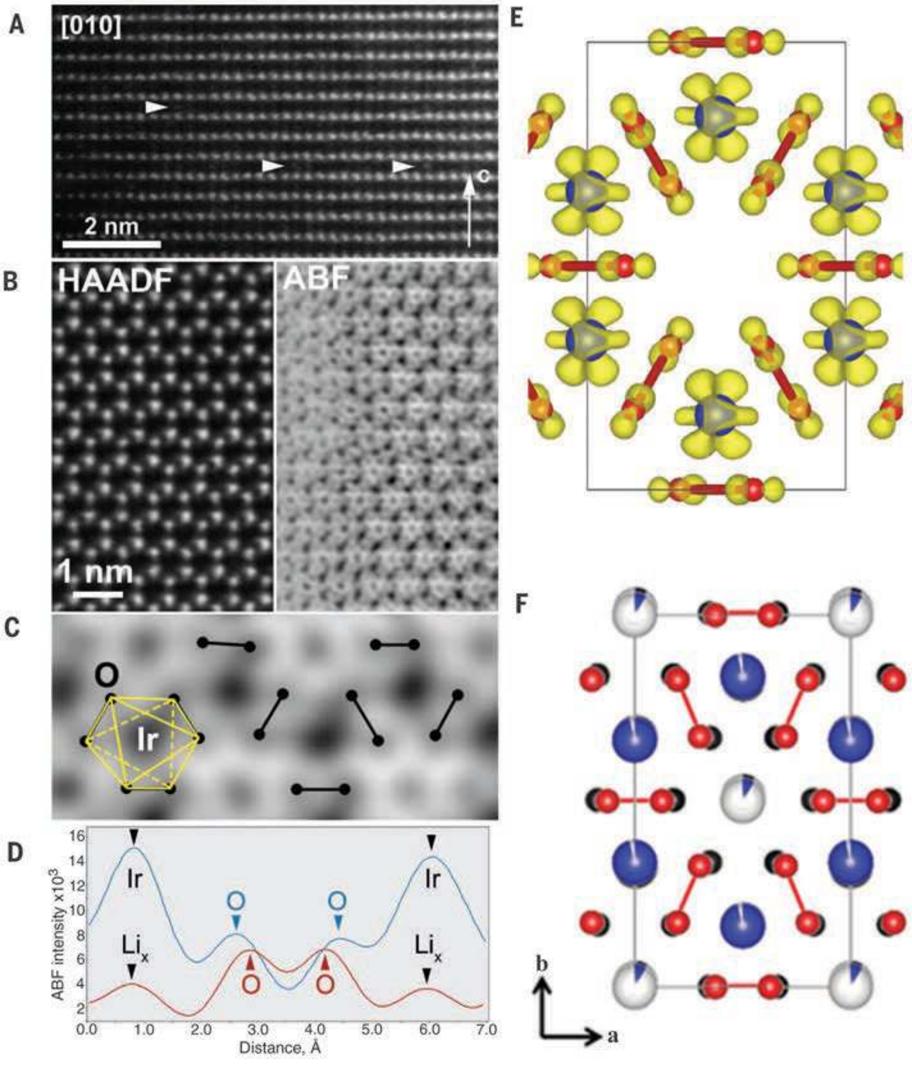

Fig. 3. Structural changes in the oxygen sublattice. (**A**) [010] HAADF-STEM image of the charged Li$_{0.5}$IrO$_3$ sample, demonstrating the ordered sequence of the Ir layers corresponding to the O1-type structure. The hexagonal close-packing is evident from the absence of the lateral displacement of layers. Virtually no migration of the Ir cation to the Li layers is observed; a few antisite point defects are marked with arrowheads. (**B**) [001] HAADF-STEM and ABF-STEM images of the same sample (taken from different areas; the noise in the ABF-STEM image is suppressed by applying a low-pass Fourier filter). (**C**) Enlarged ABF-STEM image. O-O pairs with short projected distances are marked with dumbbells. The O-O pairs arise from twisting the opposite triangular faces of the IrO$_6$ octahedra (shown in yellow). (**D**) ABF intensity profiles along the O-O pairs with long (blue) and short (red) projected distances. (**E**) [001] projection of the Li$_{0.5}$IrO$_3$ in the O1 stacking configuration, obtained with DFT calculations. Li atoms are omitted for clarity, oxygen atoms are shown in red, and Ir atoms are in blue. The yellow surfaces are the Fukui orbitals. (**F**) Structure of the charged Li-Ir-O material, as obtained from neutron powder diffraction (fit shown in fig. S5), overlaid on the pristine structure (fit in fig. S10) shown in black, clearly illustrating the formation of O-O dimers. The overlay required shrinking the pristine structure slightly, but the aspect ratio was unaltered.

of peroxo species therefore manifests itself as a distortion of the oxygen framework with the formation of shorter and longer O-O distances.

An important aspect of these materials is the extent to which they allow O_2 recombination and subsequent oxygen gas release during oxidation, which must be minimized to reduce the irreversible capacity loss. Figure S12 shows that the oxygen release here is relatively small, especially for Li_2IrO_3, and only occurs at voltages above 4.3 V versus Li/Li^+, consistent with our previous studies (*13*, *16*, *19*). This voltage corresponds to ~1.3 V versus standard hydrogen electrode, very close to the potential at which water is split (1.23 V). Our value is a rough estimate, but it does suggest that peroxo-species will be stable against formation of oxygen gas if they form below 4.3 V. This explains why irreversible capacities have plagued the Li-rich NMC materials, which must be oxidized up to 4.5 V to convert to an S curve.

Figure 4A shows a steady decrease in capacity (with no associated voltage fade) during extended cycling, with ~50% retention after only 50 cycles. This fade coincides with the structural variations resulting in the changes to the XRD patterns in Fig. 1. Figure 4 shows the structural changes that occur during extended cycling, as visualized with HAADF-STEM imaging. The image collected after 50 cycles is very unusual, with an apparent nanoscale intergrowth of two distinct structures. The structural changes during electrochemical cycling that involve the gliding of $(Ir_{1-x}Sn_x)_{2/3}O_2$ slabs against each other are ultimately detrimental to the long-term cycling of this material, thus giving rise to capacity fade without any of the voltage fade seen in other Li-rich materials. This demonstrates that these two parameters for evaluating battery performance are not directly related here and that although the transformation from O3 to O1 structures prevents voltage fade, it still results in detrimental capacity fade.

Table 1. Average O-O distances obtained by DFT, NPD, and TEM. "Short" refers to two oxygen atoms between two nearest-neighbor Ir atoms, as viewed in the [001] projection in Fig. 3, E and F. "Long" refers to distances at which the oxygen atoms lie between an Ir atom and a vacancy. In all cases, the distances are averages for the structure. Projected distances are shown for the O1 structure only. N/A, not applicable; ND, not determined.

Sample	O-O distance (Å)		O-O distance in [001] projection (Å)	
	Short	Long	Short	Long
Li_2IrO_3				
Neutron	2.77(2)	2.84(2)	N/A	N/A
DFT	2.74	2.89	N/A	N/A
$Li_{0.5}IrO_3$				
Neutron	2.45(2)	2.73(4)	1.42(1)	1.86(3)
DFT	2.54	2.77	1.51	1.88
TEM	ND	ND	1.56	1.83
$LiNi_{1/3}Mn_{1/3}Co_{1/3}O_2$*	2.686	2.686	N/A	N/A
$Li_{0.04}Ni_{1/3}Mn_{1/3}Co_{1/3}O_2$*	2.553	2.553	N/A	N/A

*From (*28*), as an indication of behavior in systems where redox involves the cationic species only.

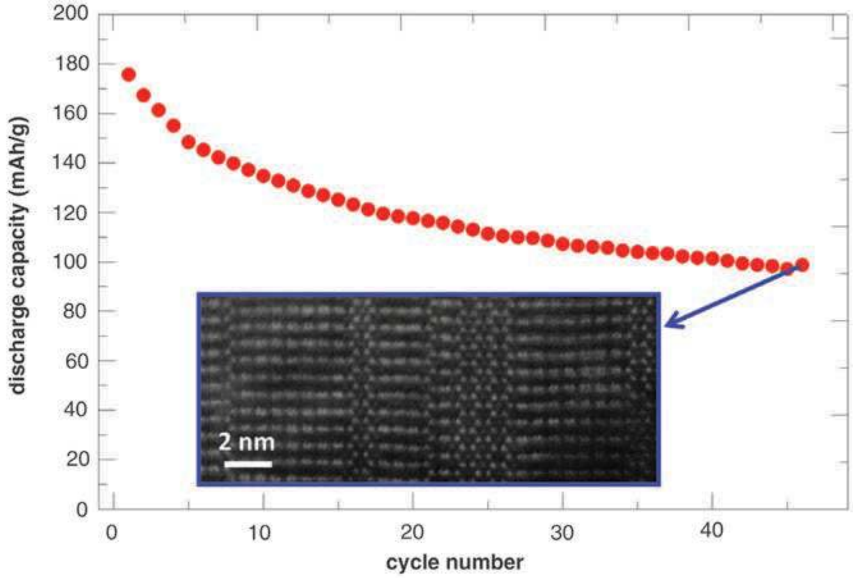

Fig. 4. Long-term cycling performance. Discharge capacity during extended cycling for $Li_2Ir_{0.75}Sn_{0.25}O_3$. (**Inset**) [100] HAADF-STEM image of a particle obtained after 50 cycles, showing complex nanoscale structuring.

Our NPD and DFT results suggest that peroxo-like dimers form uniformly throughout the bulk in the fully charged $Li_{0.5}IrO_3$ material, allowing us to determine the possible limits on the value of the formal charge n for peroxo-like O_2^{n-} dimers. The lower bound can be set by assuming that all of the 1.5 Li atoms transferred per O_3 unit are attributed to oxygen redox only; this yields $n = 3.0$. The upper bound is set by assuming the mixed redox obtained by DFT calculations (and confirmed qualitatively with XPS), in which case the oxygen lattice accounts for ~1.0 Li atom removed per O_3 unit, resulting in $n = 3.3$. This study therefore suggests the formation of predominantly O_2^{3-} species in Li-rich layered oxides, which explains why all of the lithium cannot be systematically removed from these materials simply by fully oxidizing the oxygen, as would be the case if $n = 2$ was accessible. This also explains why the peroxo-like species were detected by electron paramagnetic resonance (EPR) (*13*, *30*), given that O_2^{2-} is EPR silent whereas O_2^{3-} is active.

The fact that the formation of peroxo-like dimers does not necessarily imply antisite cation disordering has a few consequences. In Li_2IrO_3, the displacement of oxygen atoms during first charge results in confining the space around the iridium atom (Fig. 3F). This results in less free volume around each iridium atom and more tight binding to the surrounding oxygen atoms, therefore lending support to the fact that little migration of iridium takes place and no conversion to the S curve is seen. By contrast, the disorder caused by the addition of tin locally disrupts the pattern of the O_2^{n-} species promoting such migration, which results in a far greater abundance of the antisite defects in the [010] HAADF-STEM images of the charged $x = 0.25$ sample (fig. S13). Thus, conversion to an S curve is seen. More generally, once the Li is removed from the transition metal layers in all Li-rich oxides, the created free volume promotes migration to the Li layer. The microscopy images for this model system also show that these high capacities can be achieved for single-phase layered materials and do not necessarily require structural intergrowth of two layered phases, as proposed in the past (*3*). Lee *et al.* (*31*) showed Li-rich Li-Cr-Mo-O materials that convert toward a disordered rock salt structure during charge (corresponding to massive cation migration such that the transition metal and lithium layers are indistinguishable). Unfortunately, this study did not examine the redox processes involved, and we propose that this material is simply another example of the Li-rich oxides where oxygen participation in the redox process leads to high capacities.

Metal substituents can be used to tune the physical properties of these Li-rich phases because they affect the $(O_2)^{n-}$ stability against oxygen recombination or voltage fade, as previously demonstrated for $Li_2Ru_{1-x}M_xO_3$ (M = Sn, Ti, Mn). The benefits of Sn, in that it limits both $O_{2(g)}$ release and voltage fade, are preserved in the $Li_2Ir_{1-y}Sn_yO_3$ system but are mitigated by the emergence of a capacity fade mechanism that is linked to the emergence and accumulation of stacking faults. This finding emphasizes that the origins of voltage and capacity fading in these Li-rich layered phases are different, a point that has previously been a source of confusion.

In summary, combined TEM, neutron diffraction, and ab initio studies on high-capacity Li-rich $Li_2Ir_{1-x}Sn_xO_3$ layered phases permitted the atomic-scale visualization of the $(O\text{-}O)^{n-}$ peroxo-like dimers responsible for the capacity gain in Li-rich layered electrode materials. These observations lead to a better understanding of peroxo formation and localization, O_2 recombination, and the effect of the transition metal substituents. Additionally, these findings provide a chemical handle for tuning the performances of Li-rich layered materials.

REFERENCES AND NOTES

1. B. L. Ellis, K. T. Lee, L. F. Nazar, *Chem. Mater.* **22**, 691–714 (2010).
2. Z. Lu, L. Y. Beaulieu, R. A. Donaberger, C. L. Thomas, J. R. Dahn, *J. Electrochem. Soc.* **149**, A778 (2002).
3. M. M. Thackeray, C. S. Johnson, J. T. Vaughey, N. Li, S. A. Hackney, *J. Mater. Chem.* **15**, 2257–2267 (2005).
4. J. M. Tarascon *et al.*, *J. Solid State Chem.* **147**, 410–420 (1999).
5. G. Ceder *et al.*, *Nature* **392**, 694–696 (1998).
6. M. K. Aydinol, A. F. Kohan, G. Ceder, K. Cho, J. Joannopoulos, *Phys. Rev. B* **56**, 1354–1365 (1997).
7. C.-C. Chang, O. I. Velikokhatnyi, P. N. Kumta, *J. Electrochem. Soc.* **151**, J91–J94 (2004).
8. J. Graetz, C. C. Ahn, R. Yazami, B. Fultz, *J. Phys. Chem. B* **107**, 2887–2891 (2003).
9. S. Laha *et al.*, *Phys. Chem. Chem. Phys.* **17**, 3749–3760 (2015).
10. H. Koga *et al.*, *J. Phys. Chem. C* **118**, 5700–5709 (2014).
11. M. Oishi *et al.*, *J. Power Sources* **276**, 89–94 (2015).
12. W.-S. Yoon *et al.*, *J. Phys. Chem. B* **106**, 2526–2532 (2002).
13. M. Sathiya *et al.*, *Nat. Mater.* **12**, 827–835 (2013).
14. M. Sathiya *et al.*, *Nat. Mater.* **14**, 230–238 (2015).
15. M. Sathiya *et al.*, *Chem. Mater.* **25**, 1121–1131 (2013).
16. E. McCalla *et al.*, *J. Electrochem. Soc.* **162**, A1341–A1351 (2015).
17. J. Rouxel, *Chem. Eur. J.* **2**, 1053–1059 (1996).
18. M. Sathiya *et al.*, *Chem. Commun.* **49**, 11376–11378 (2013).
19. E. McCalla *et al.*, *J. Am. Chem. Soc.* **137**, 4804–4814 (2015).
20. A. R. Armstrong *et al.*, *J. Am. Chem. Soc.* **128**, 8694–8698 (2006).
21. N. Yabuuchi *et al.*, *Proc. Natl. Acad. Sci. U.S.A.* **112**, 7650–7655 (2015).
22. Materials and methods are available as supplementary materials on *Science* Online.
23. H. Kobayashi, M. Tabuchi, M. Shikano, H. Kageyama, R. Kanno, *J. Mater. Chem.* **13**, 957–962 (2003).
24. S. D. Findlay *et al.*, *Ultramicroscopy* **110**, 903–923 (2010).
25. R. Ishikawa *et al.*, *Nat. Mater.* **10**, 278–281 (2011).
26. L. Gu, D. Xiao, Y.-S. Hu, H. Li, Y. Ikuhara, *Adv. Mater.* **27**, 2134–2149 (2015).
27. D. Batuk, M. Batuk, A. M. Abakumov, J. Hadermann, *Acta Crystallogr. B* **71**, 127–143 (2015).
28. S. C. Yin, Y. H. Rho, I. Swainson, L. F. Nazar, *Chem. Mater.* **18**, 1901–1910 (2006).
29. F. Grasset, C. Dussarrat, J. Darriet, *J. Mater. Chem.* **7**, 1911–1915 (1997).
30. M. Sathiya *et al.*, *Nat. Commun.* **6**, 6276 (2015).
31. J. Lee *et al.*, *Science* **343**, 519–522 (2014).

ACKNOWLEDGMENTS

E.M. thanks the Fonds de Recherche du Québec–Nature et Technologies and ALISTORE–European Research Institute for funding this work, as well as the European community I3 networks for funding the neutron scattering research trip. This work was also funded by the Slovenian Research Agency research program P2-0148. This work is partially based on experiments performed at the Institut Laue Langevin. We thank J. Rodriguez-Carvajal for help with neutron scattering experiments and for fruitful discussions. We also thank M. T. Sougrati for performing the Sn-Mössbauer measurements. Use of the Advanced Photon Source at Argonne National Laboratory was supported by the U.S. Department of Energy, Office of Science, Office of Basic Energy Sciences, under contract no. DE-AC02-06CH11357. M.S. and M.-L.D. acknowledge high-performance computational resources from GENCI-CCRT/CINES (grant cmm6691). J.-M.T. acknowledges funding from the European Research Council (ERC) (FP/2014-2020)/ERC Grant-Project670116-ARPEMA.

Supplementary Materials for

Visualization of O-O peroxo-like dimers in high-capacity layered oxides for Li-ion batteries

Eric McCalla, Artem M. Abakumov, Matthieu Saubanère, Dominique Foix, Erik J. Berg, Gwenaelle Rousse, Marie-Liesse Doublet, Danielle Gonbeau, Petr Novák, Gustaaf Van Tendeloo, Robert Dominko, Jean-Marie Tarascon*

*Corresponding author. E-mail: jean-marie.tarascon@college-de-france.fr

This PDF file includes:

- Materials and Methods
- Figs. S1 to S13
- Tables S1 and S2
- Full Reference List

Materials and Methods

Synthesis

The current study involved the synthesis of three materials: $Li_2Ir_{1-x}Sn_xO_3$ with x = 0, 0.25 and 0.5. All samples were prepared by first mixing lithium carbonate (Li_2CO_3, Sigma Aldrich 99%), iridium oxide (IrO_2, Alfa Aesar, 99%) and tin oxide (SnO_2, Sigma Aldrich 99.9%) in a high energy SPEX 800 ball mill for 40 minutes. The mixtures included 10% excess lithium in order to compensate for lithium loss during heating. Two heating steps were used: a 12 h hold at 1000 °C (heated at 5 °C/min), and a 36 h hold at 900 °C (cooled by turning off the furnace). Between each step the samples were ground and pressed back into a pellet. Approximately 3-5 g of each sample were made.

Electrochemistry

Electrochemical studies were carried out in Swagelok type cells with Li metal counter electrode and LP30 electrolyte (BASF) which were assembled in an argon filled glove box. The active material was ball milled with 20% Wt. carbon black (Super P, Timcal) using the SPEX ball mill for 20 minutes. Galvanostatic cycling was performed at either C/10, or C/20 (C-rate here is defined to be the rate required to remove 1 Li from $Li_2Ir_xSn_{1-x}O_3$). It was also found that this material cycled well without carbon black, such that materials used to prepare the ex situ sample for neutron diffraction contained no carbon black.

X-ray and Neutron Powder Diffraction

X-ray powder diffraction (XRD) patterns of the pristine samples and ex situ samples were recorded using a BRUKER D8 Advance diffractometer using Cu-Kα radiation. The crystallographic parameters were determined by either Rietveld refinement using the Rietica software (version 2.1) in cases where stacking faults were minimal, otherwise FAULTS (*32*) was used. The values for *a, b, c* reported with FAULTS correspond to the monoclinic lattice parameters as used in typical Rietveld refinements and to the interplanar distance between TM layers, respectively, as detailed in (33). The Li_2IrO_3 samples (both pristine and ex situ) were also studied using synchrotron X-ray powder diffraction at Argonne National Laboratories' 11-BM beamline. An in situ XRD experiment was performed on Li_2IrO_3 using the Bruker D8 diffractometer. High resolution neutron powder diffraction experiments were also performed on the pristine Li_2IrO_3 material and on this same material charged to 4.5 V (removal of 1.5 Li per formula unit). Measurements were made on the D1B neutron powder diffractometer at Institut Laue Langevin (ILL, Grenoble, $\lambda = 1.28618$ Å). The 1.5 g charged sample was prepared in a large Swagelok cell by cycling a cell with active material only as the positive electrode up to 4.5 V at C/20 and then holding at 4.5 V until 1.5 total lithium atoms per stoichiometric unit were removed.

Transmission Electron Microscopy

Transmission electron microscopy was performed on the fully charged Li_2IrO_3 and $Li_2Ir_{0.75}Sn_{0.25}O_3$ samples, as well as the latter after 50 cycles. Each TEM specimen was prepared in the glove box by crushing the crystals with hexane in a mortar and depositing drops of the suspension onto holey carbon grids. The sample was transported to the microscope column completely excluding contact with air. High angle annular dark field scanning transmission electron microscopy (HAADF-STEM) and annular bright field STEM (ABF-STEM) images were obtained with aberration-corrected Titan G^3 electron microscope operated at 200 kV.

X-ray Photoelectron Spectroscopy

X-ray photoelectron spectroscopy (XPS) measurements were carried out with a Kratos Axis Ultra spectrometer, using a focused monochromatic Al-Kα radiation (hν=1486.6 eV). The XPS spectrometer was directly connected through a transfer chamber to an argon-filled dry box, in order to avoid moisture/air exposure of the samples. For the Ag3d$_{5/2}$ line, the full width at half maximum (FWHM) was 0.58 eV under the recording conditions. Peaks were recorded with a constant pass energy of 20 eV. The pressure in the analysis chamber was around 5.10^{-9} mbar. The binding energy scale was calibrated from the hydrocarbon contamination using the C1s peak at 285.0 eV. Core peaks were analysed using a nonlinear Shirley-type background. The peaks positions and areas were optimized using a weighted least-squares fitting method with 70% Gaussian and 30% Lorentzian line shapes. We focus here on the core peaks only. A minimum number of components were used in order to fit the experimental curves. For each set of samples the curve fits were obtained using fixed FWHM, the degrees of freedom being limited to the binding energies and amplitudes. For estimation of the uncertainty in the peroxo fraction, the O1s spectrum of each pristine sample was fitted two different ways: with three components as reported in the main text and with four components as for the fully charged samples where peroxo-like species are present in significant quantities. Since no peroxo is present in the pristine samples, this gives us an estimate of XPS detection limit for peroxo species (~2 % here) and allows the determination of the uncertainty on the peroxo fractions in the scans after electrochemical cycling (error bars in Figs. 2d and S4). In an upcoming publication the valence band spectra will be analysed to more closely explore the changes in Ir during electrochemical cycling.

Mössbauer Spectroscopy and Differential Scanning Mass Spectrometry

In situ Sn Mössbauer spectroscopy of $Li_2Ir_{0.75}Sn_{0.25}O_3$ was performed as described in detail in (*34-35*). ^{119}Sn Mossbauer spectra were collected with a constant acceleration spectrometer using a Ca^{119m}SnO$_3$ source in the transmission geometry. The hyperfine parameters: IS (isomer shift) and QS (quadrupole splitting) were obtained by fitting the data with lorentzian functions. The cell was cycled at a C/30 rate at room temperature.

The amount of oxygen and carbon dioxide released during electrochemical cycling was obtained using differential electrochemical mass spectrometry (DEMS). The configuration has been described elsewhere (*19*) while the electrode preparation method and experimental details are included in Ref. 36. The cell was cycled in galvanostatic mode at ~C/25 in a potential window of 2.5 - 4.6 V with the gases evolved being probed in 15 min intervals.

Density Functional Theory

Density functional theory (DFT) calculations were performed to model the Li_yIrO_3 structure as a function of lithium content, y. All calculations were performed using the plane-wave density functional theory (DFT) code from the Vienna *Ab initio* Simulation Package (VASP, version 5.3).(*37, 38*) Spin-dependent calculations were performed using the generalized gradient approximation of Perdew, Burke, and Ernzerhof (PBE) (*39*) including Hubbard-U corrections following the rotationally invariant formalism of Dudarev.(*40*) The electron wavefunctions were described in the projected augmented wave formalism (PAW) (*41, 42*), the plane wave energy cutoff was set to 600 eV and the Brillouin zone integration was done in a k-point grid distributed as uniformly as possible, using Monkhorst-Pack meshes of 6 x 4 x 4. Calculations were performed with starting configurations in the *C2/m* space group with the O3 stacking (Li contents of 2, 1, 0.5 and 0 were used). Calculations were also performed for the O1 stacking with Li-content 0.5 (the only configuration which remained in the O1 structure was for Li on the 2c site (0, 0, 0.5) as determined experimentally from XRD and neutron powder diffraction patterns. In all cases, all Ir atoms begin in a perfect honeycomb lattice on the transition metal layer. All atom coordinates and lattice parameters were fully relaxed until the forces acting on each atom were less than 1.10^{-3} eV/Å². Let it be noted that we focus in this paper on the two structures giving closest agreement with experimental lattice parameters for the pristine (y = 2) and charged (y = 0.5) structures only. In both cases, these best structures were obtained with both U = 2 and 4 eV and assuming ferromagnetic ordering. In an upcoming publication, the breadth of methods used, including the inclusion of spin-orbit coupling for all structures will be presented in detail. For the y = 2 material (pristine), the results presented in Fig. S8 with U = 2 eV give lattice parameters: *a* = 5.244 Å, *b* = 8.764 Å, *c* = 5.205 Å, β = 110.35°, yielding a 1.3 % cell volume error compared to the experimental results in Table S1. For the charged sample, $Li_{0.5}IrO_3$, the DFT calculations resulted in *a* = 5.199 Å, *b* =9.011 Å, *c* = 4.615 Å in the O1 structure (β = 90°) and a 2.7 % error for the cell volume as compared to the unit cell obtained based on the 11-BM synchrotron data in Fig. S5 (note that the U = 4 eV calculations yielded a 2.1 % error for this structure). As discussed in the main text, Fukui functions represent the electronic response of the system to an oxidation or reduction and are a useful way to probe changes in the electronic structure during electrochemical cycling. The Fukui functions are calculated based on two different self-consistent DFT calculations at N and N + ε electrons (N is the number of electrons per unit cell and ε is an infinitesimal variation which can either be negative (electrons) or positive (holes)); these calculations include all polarisation effects due to charge variation. In that sense they are not uniquely probes for the highest occupied and lowest unoccupied electronic levels of the system. The Fukui function is then obtained by subtracting the two electron densities. The function shown in the main text was obtained using a positive ε with the U = 4 eV structure, though the function obtained with a negative value is very similar (qualitatively consistent with a half full σ^* orbital).

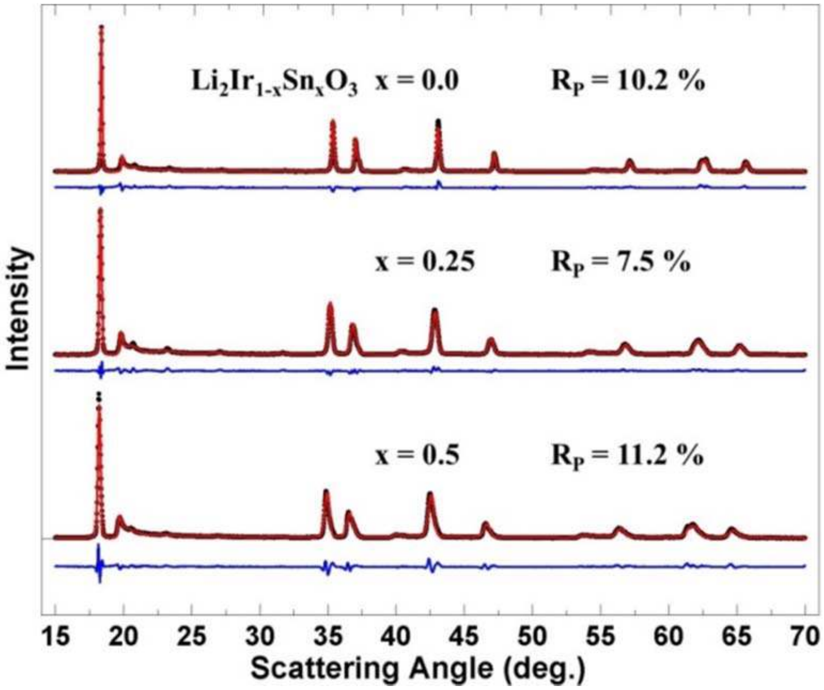

Fig. S1: XRD fits for all pristine samples using FAULTS to refine the patterns taking stacking faults into account. A selected zoom of this figure is included in Fig. 1 of the main text.

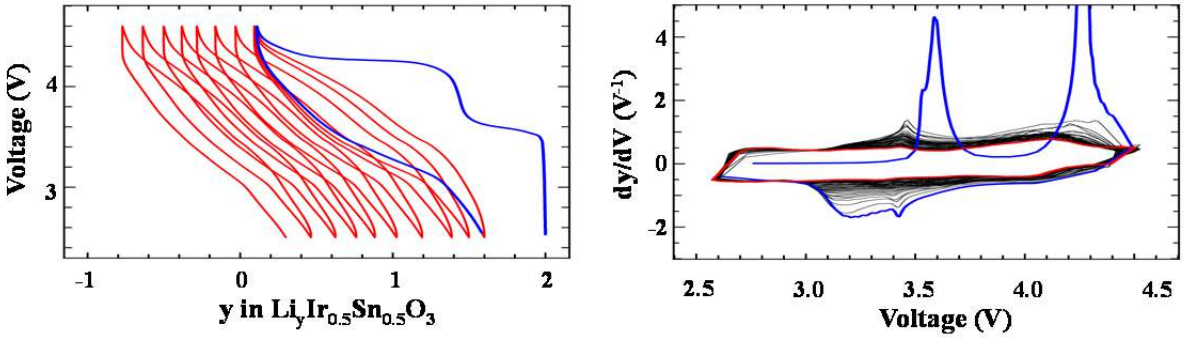

Fig. S2: Electrochemical data for the sample with 50 % substitution of Ir with Sn. The behavior is very similar to that of the 25 % substituted sample given in Fig. 1 with a more pronounced conversion to the signature S-curve in the voltage profile.

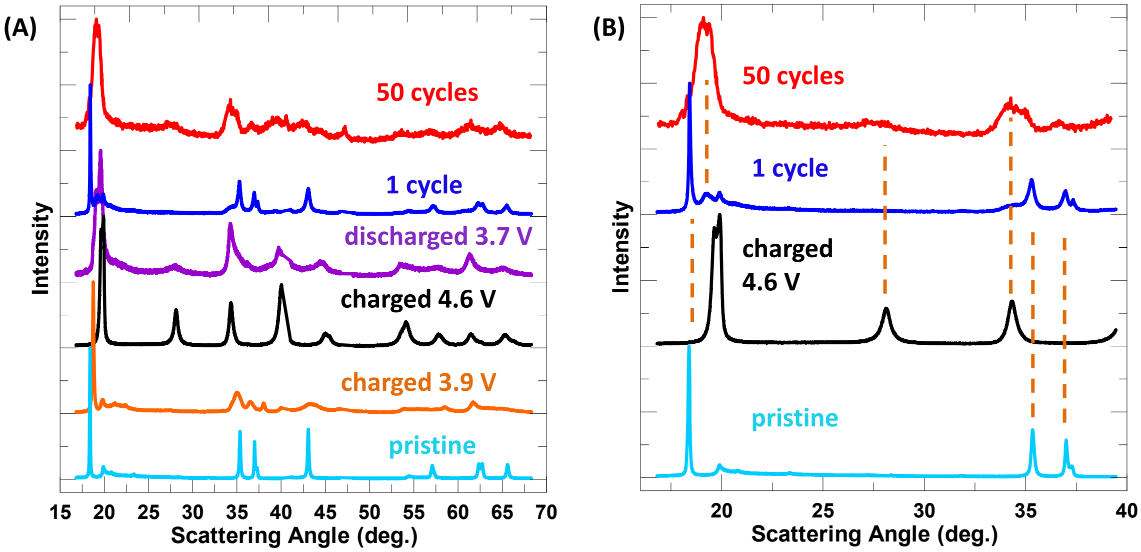

Fig. S3: Ex situ XRD data obtained for Li_2IrO_3 at various states of charge. Right: zoom to show the appearance of small amounts of the new phase as early as the end of the first cycle. All scans obtained with synchrotron XRD (scattering angle recalculated to correspond to Cu-Kα radiation), except for the 50 cycles sample, measured on the Bruker diffractometer.

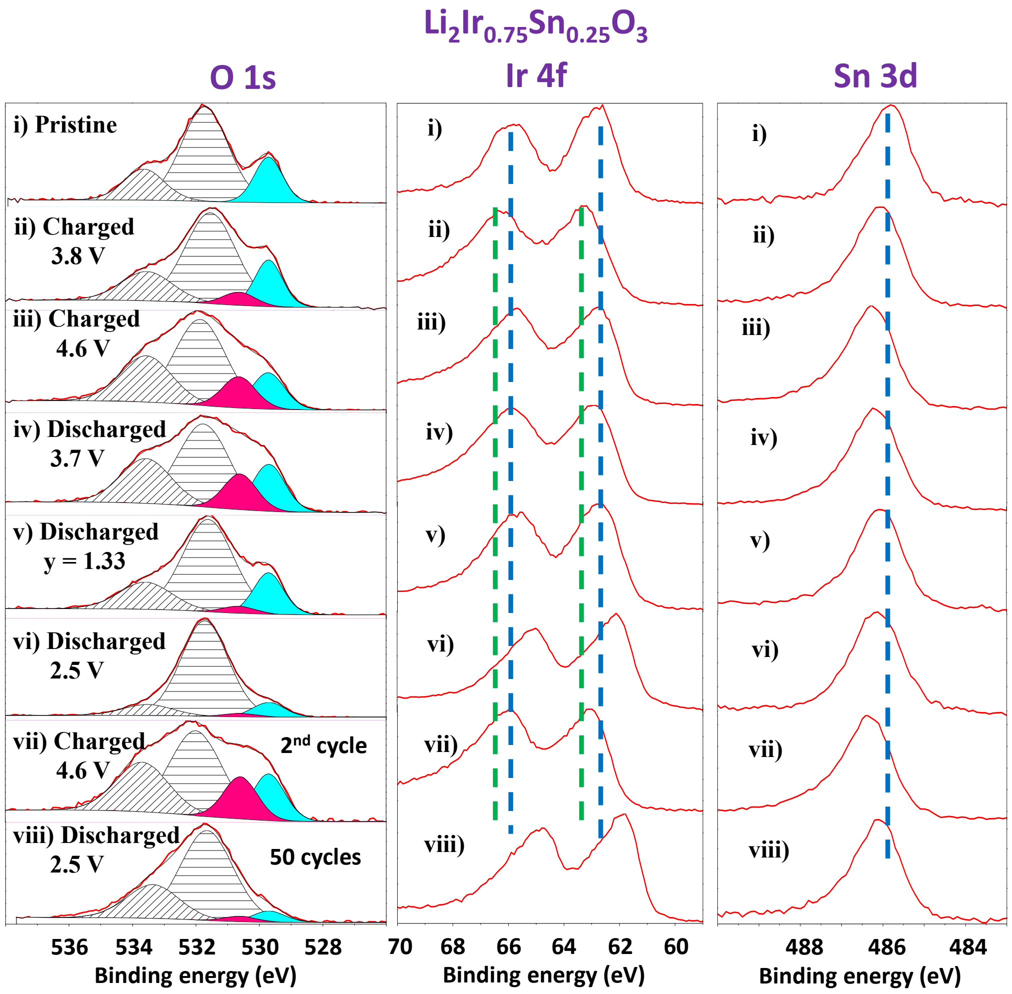

Fig. S4: XPS results for $Li_2Ir_{0.75}Sn_{0.25}O_3$ at various points after electrochemical cycling. The O^{2-} (blue) and O_2^{n-} (red) peaks are attributed to the sample, while the two grey peaks are attributed to surface species and electrolyte decomposition products as described in (13). In order to track the progress of the peroxo species during cycling, all O 1s spectra (except the pristine) were fit here assuming all four peaks are present. For the Ir 4f core peaks, the dashed lines are guides for the eye indicating the position of the pristine (4+) peaks in blue and the highest oxidation state (formally 5+) in green. The shift in the Sn peak is attributed to changes in the Sn environment.

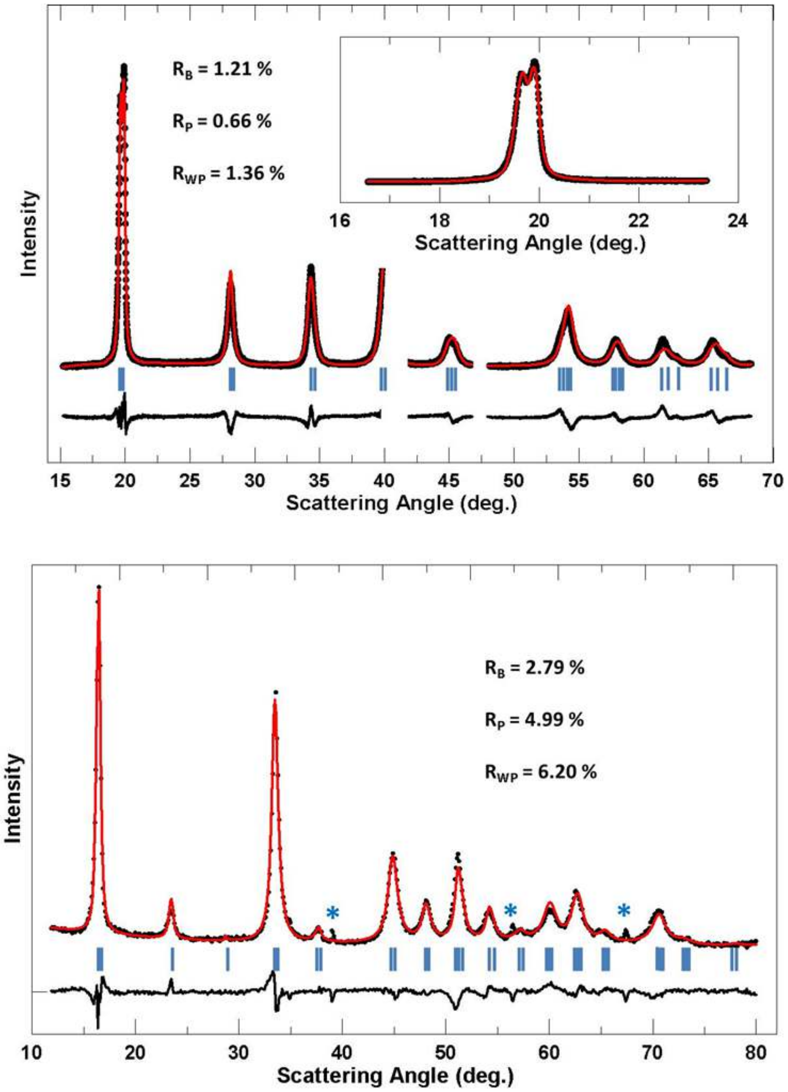

Fig. S5: Neutron (bottom) and synchrotron XRD (top, scattering angle recalculated to correspond to Cu-kα radiation) data with fits for Li_2IrO_3 charged to 4.6 V (extraction of 1.5 Li per formula unit). Contaminant peaks from the adhesive used to keep the sample in place have been omitted from the XRD pattern. * indicates small sharp peaks attributed to products of electrolyte oxidation in the neutron pattern where carbon and oxygen contribute significantly.

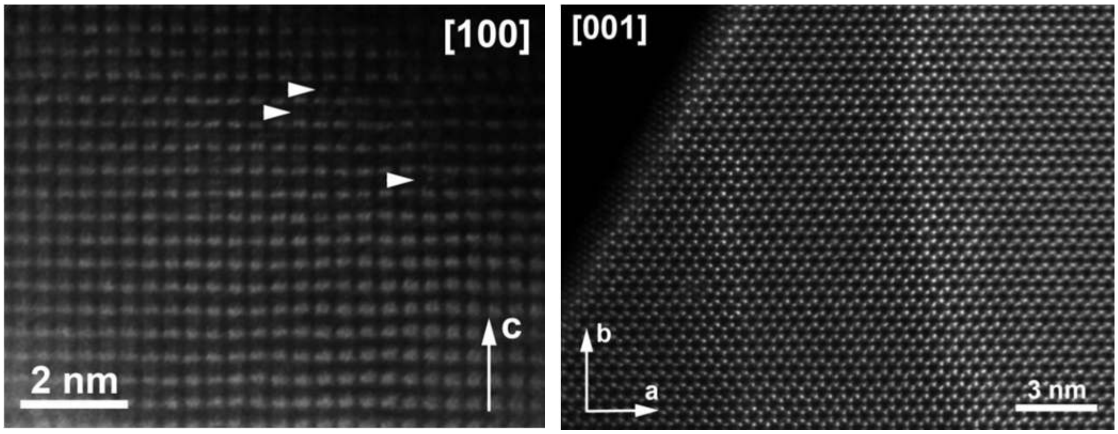

Fig. S6: Left: [100] HAADF-STEM image of the charged $Li_{0.5}IrO_2$ sample showing the cation ordering in the transition metal layers. The Ir columns are projected as pairs of bright dots separated by ~0.14 nm. Some antisite defects with the Ir atoms at the vacant Li layers are indicated with arrows. Right: [001] HAADF-STEM image of perfect "honeycomb" ordering.

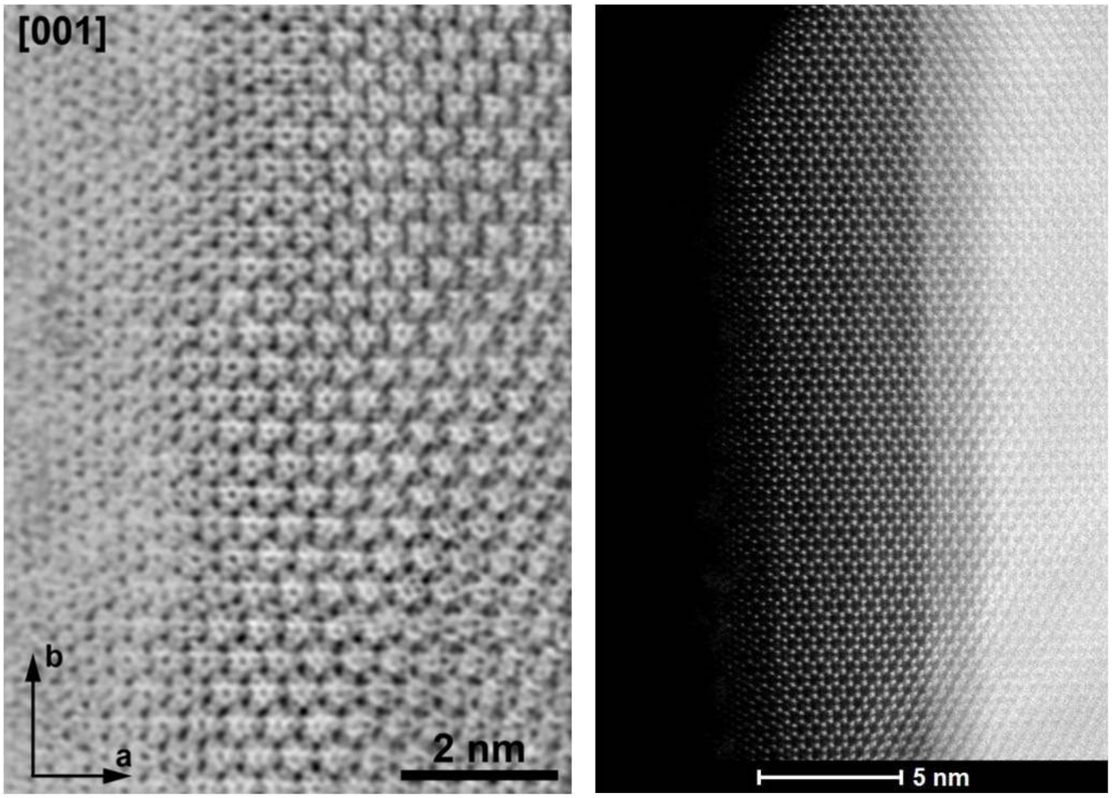

Fig. S7: Overview [001] ABF-STEM image of the charged $Li_{0.5}IrO_2$ sample (left). The noise in the ABF-STEM image is suppressed by applying a low-pass Fourier filter. The right panel shows the [001] HAADF-STEM image of the same area.

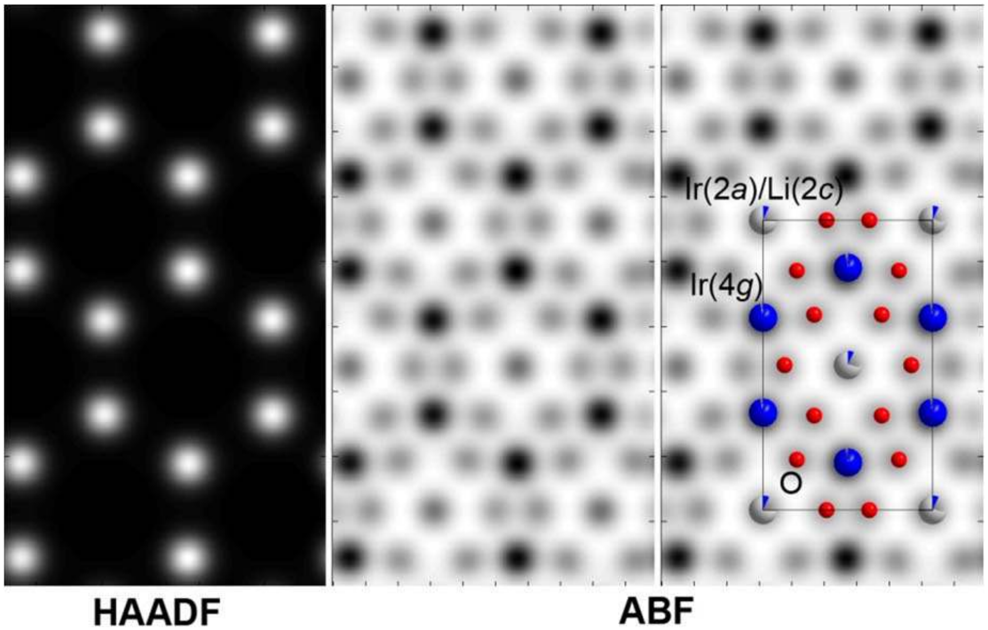

Fig. S8: Simulated [001] HAADF-STEM and ABF-STEM images of the charged $Li_{0.5}IrO_2$ sample calculated with the multislice method using the QSTEM software (43) (thickness 4.7 nm). The atomic positions from the NPD refinement (Table S2) are overlaid in the ABF-STEM pattern at the right. Short and long projected O-O separations are clearly visible in the ABF-STEM image. Note that the Li (2*c*) position provides the contrast in the ABF-STEM image which is as strong as the contrast corresponding to the O columns. This is because of overlap with the Ir(2*a*) position containing 7% Ir, which in total provides the average scattering density close to that of the oxygen atom.

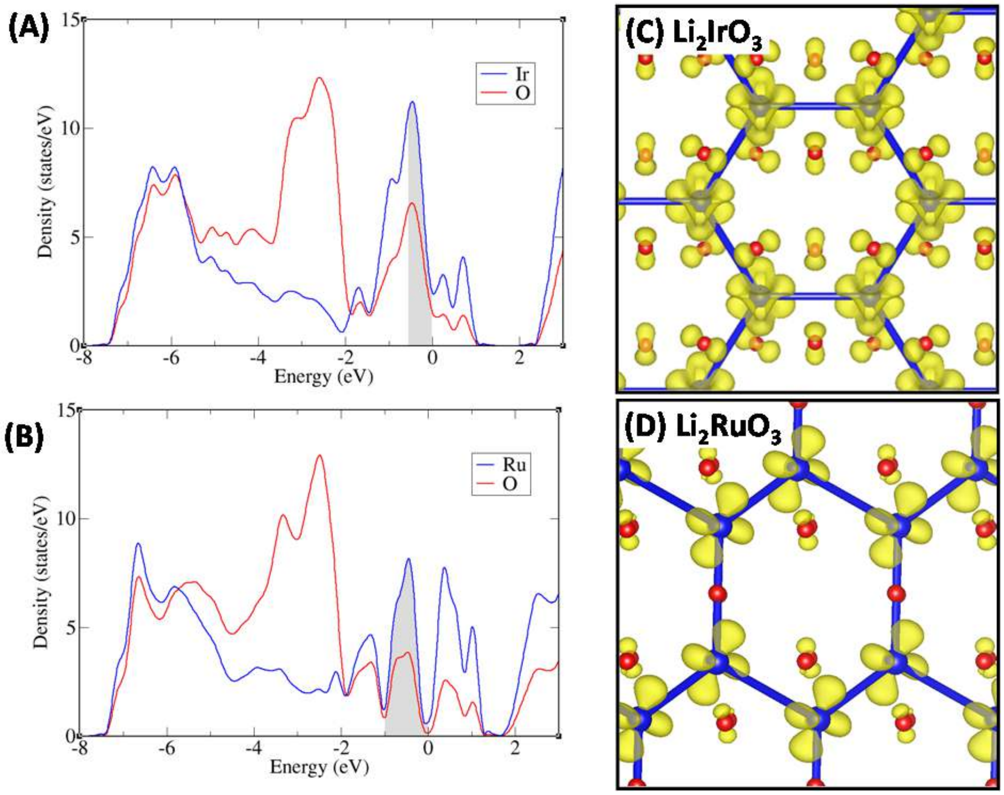

Fig. S9: DFT calculation results for Li_2IrO_3 (A, C) and Li_2RuO_3 (B, D). The density of states (DOS) are shown in a and b (all are summations of spin up and spin down DOS values). The grey areas indicate the DOS that would be emptied if two electrons were removed considering the band rigid approximation (i.e. without any electronic rearrangements). The Fukui functions (obtained with a negative ε value, hole creation) are shown in C and D. The DOS results show a greater involvement of oxygen in the case of the Ir-based material at the start of charge. The Fukui functions also highlight the presence of Ru-Ru dimers in Li_2RuO_3 resulting in Ru-Ru π-bonding. For the Ir-based material, the bonding is primarily limited to Ir-O bonds.

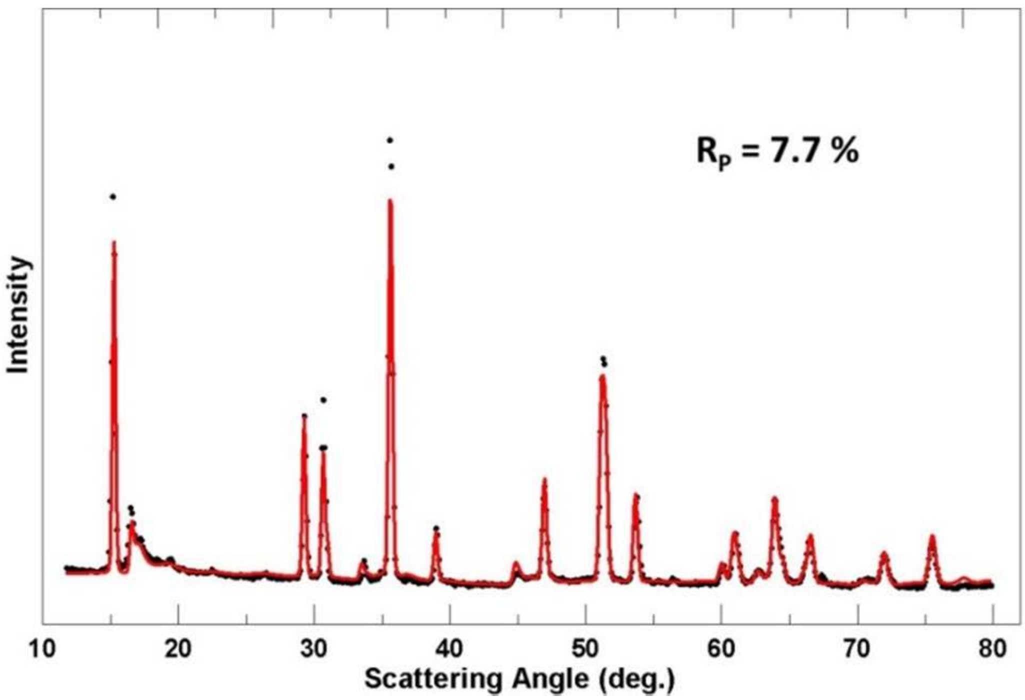

Fig. S10: Neutron diffraction pattern and fit for the pristine Li_2IrO_3 performed with FAULTS taking stacking faults into account.

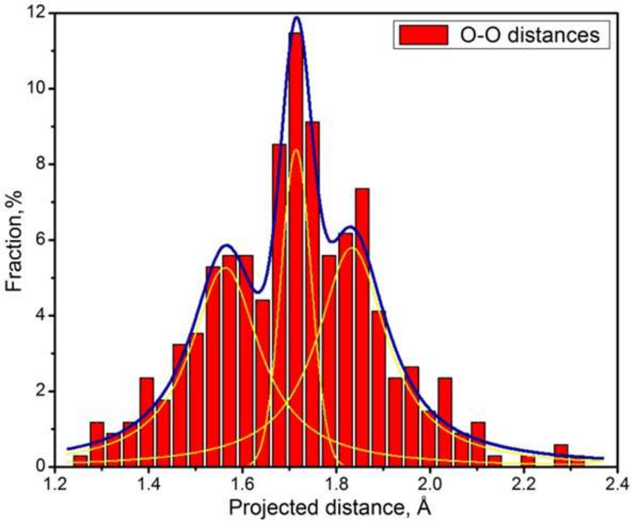

Fig. S11: Histogram of O-O projected distances measured using the [001] ABF-STEM image of the Li_2IrO_3 sample in the fully charged state. The data is a fit using a tri-modal distribution with peaks centered at 1.56, 1.71 and 1.83 Å. The short and long projected lengths correspond nicely to the O-O projected distances expected for peroxo-like dimers from both DFT calculations and neutron diffraction. Moreover, if the peroxo-like dimers form throughout the material the short O-O distances should account for 1/3 of all O-O distances as they do in the distribution here, such that the intermediate distances at 1.71 Å would also be a consequence of the shortened O-O dimers. As the charged sample is not fully oxidized it is feasible that some oxygen atoms remain in the pristine O^{2-} state and thereby also contribute to this central peak. Note that the peak at 1.56 Å cannot be rationalized without the formation of O-O dimers as discussed in the main text.

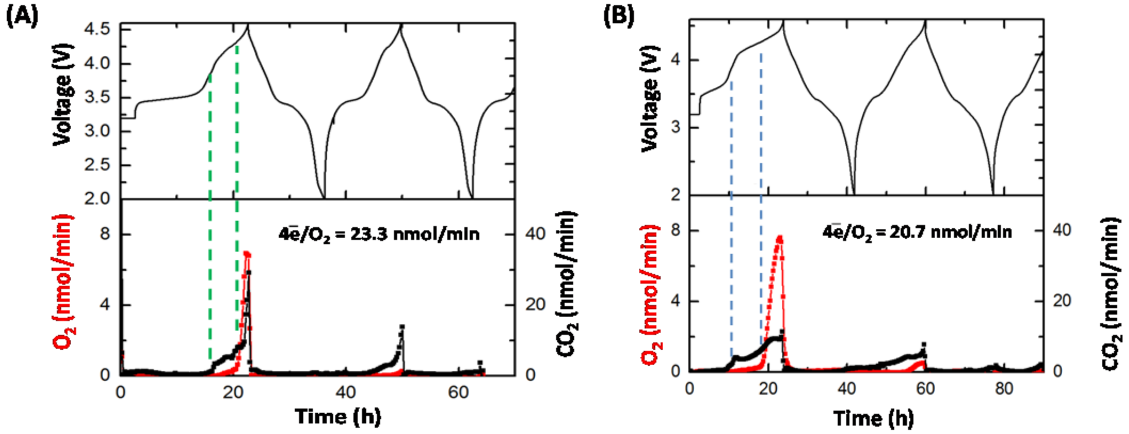

Fig. S12: Differential Electrochemical Mass Spectrometry data measuring the quantity of O_2 and CO_2 gas produced in operando for (A) Li_2IrO_3 and (B) $Li_2Ir_{0.75}Sn_{0.25}O_3$. The values quoted as 4 electrons/O_2 are an indication of the rate of oxygen gas release that would be needed in order to completely account for the current. For comparison, Ref. 16 showed a sample of Li-rich Li-Fe-Te-O where the amount of oxygen gas produced accounted for the current for much of the first charge. The levels here are considered low, and completely negligible below 4.3 V. The dashed lines are guides for the eye to help determine at which voltage the onsets of carbon dioxide and oxygen are seen.

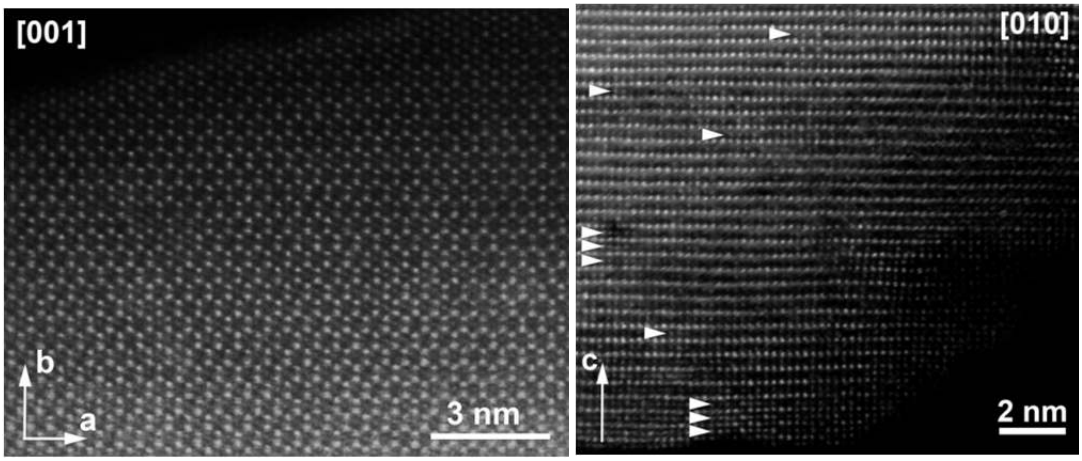

Fig. S13: [010] and [010] HAADF-STEM image of the charged x = 0.25 sample showing abundant antisite defects with the Ir atoms on vacant sites on the Li layers (some representative places are marked with arrowheads).

Table S1. Fitting parameters obtained from fitting XRD scans of the pristine $Li_2Ir_{1-x}Sn_xO_3$ samples using FAULTS as described in detail in Ref. 32. The α, β, and γ sites refer to the occupations on the three sublattices on the transition metal layer (uncertainty of 0.1 %). The values of *a, b, c* are not strictly lattice parameters in FAULTS, as there is no unit cell in such a description.

x	a (Å)	b (Å)	c (Å)	$-S_x$	α-site (%)	β-site (%)	γ-site (%)	faults (%)
0	5.1447(1)	8.9310(1)	4.8218(1)	0.16607(2)	95.8 Ir 4.2 Li	95.8 Ir 4.2 Li	91.6 Li 8.4 Ir	33.0
0.25	5.1881(2)	8.9751(1)	4.8488(1)	0.16876(4)	73.2 Ir 25 Sn 1.8 Li	73.2 Ir 25 Sn 1.8 Li	96.2 Li 3.8 Ir	33.7
0.50	5.2270(2)	9.0362(1)	4.8761(1)	0.16676(4)	83.3 Ir 14.2 Sn 2.5 Li	85.8 Sn 11.7 Ir 2.5 Li	95.0 Li 5.0 Ir	37.9
0*	5.1578(9)	8.925(1)	4.816(1)	0.1667(9)	94 Ir 6 Li	94 Ir 6 Li	88 Li 12 Ir	22.0

* Neutron diffraction results, obtained from the refinement shown in Fig. S10. Oxygen positions refined, constrained as in *C*2/*m* space group, gave the equivalent of 4*i*: (0.658(4), 0, 0.232(4)), and 8*j*: (0.176(2), 0.167(2), 0.232(4)), used in Fig. 3F.

Table S2. Neutron diffraction Rietveld fitting parameters obtained for the fully charged Li_2IrO_3 sample (composition $Li_{0.492}IrO_3$ where the lithium content was refined). Fit performed in *C*2/*m* space group, with β = 90.0°.*

a = 5.1649(4) Å	*b* = 8.8649(8) Å	*c* = 4.4469(6) Å
Site	Occupation	x, y, z
4i	100% O	0.626(4), 0, 0.224(2)
8j	100% O	0.199(2), 0.174(2), 0.224(2)
4g	96.5% Ir	0, 0.336(4), 0
2a	7% Ir	0, 0, 0
2c	98.4% Li	0, 0, 0.5

*By contrast, using synchrotron X-ray diffraction results did not constrain the oxygen positions such that they were held at the positions determined by neutron diffraction. The resulting parameter values were *a* = 5.1932(5) Å, *b* = 9.0835(9) Å, *c* = 4.4665(5) Å, y_{Ir} = 0.3201(1) and the occupation of 4*g* site was 96.1 % Ir and that of the 2*a* site was 3.9 % Ir while the 0,0,0.5 2*c* site was 100 % occupied with Li. Let it be noted that the difference in *b* lattice parameter between the neutron and XRD fits is due to this being a different sample (in-house XRD of the sample used for neutron diffraction gave *a* = 5.170(3) Å, *b* = 8.878(3) Å, *c* = 4.456(3) Å obtained on the Bruker D8 diffractometer).

References and Notes

1. B. L. Ellis, K. T. Lee, L. F. Nazar, Positive electrode materials for Li-ion and Li-batteries. *Chem. Mater.* **22**, 691–714 (2010). doi:10.1021/cm902696j

2. Z. Lu, L. Y. Beaulieu, R. A. Donaberger, C. L. Thomas, J. R. Dahn, Synthesis, structure, and electrochemical behavior of $Li[Ni_xLi_{1/3-2x/3}Mn_{2/3-x/3}]O_2$. *J. Electrochem. Soc.* **149**, A778 (2002). doi:10.1149/1.1471541

3. M. M. Thackeray, C. S. Johnson, J. T. Vaughey, N. Li, S. A. Hackney, Advances in manganese-oxide 'composite' electrodes for lithium-ion batteries. *J. Mater. Chem.* **15**, 2257–2267 (2005). doi:10.1039/b417616m

4. J. M. Tarascon, G. Vaughan, Y. Chabre, L. Seguin, M. Anne, P. Strobel, G. Amatucci, In situ structural and electrochemical study of $Ni_{1-x}Co_xO_2$ metastable oxides prepared by soft chemistry. *J. Solid State Chem.* **147**, 410–420 (1999). doi:10.1006/jssc.1999.8465

5. G. Ceder, Y.-M. Chiang, D. R. Sadoway, M. K. Aydinol, Y.-I. Jang, B. Huang, Identification of cathode materials for lithium batteries guided by first-principles calculations. *Nature* **392**, 694–696 (1998). doi:10.1038/33647

6. M. K. Aydinol, A. F. Kohan, G. Ceder, K. Cho, J. Joannopoulos, Ab initio study of lithium intercalation in metal oxides and metal dichalcogenides. *Phys. Rev. B* **56**, 1354–1365 (1997). doi:10.1103/PhysRevB.56.1354

7. C.-C. Chang, O. I. Velikokhatnyi, P. N. Kumta, Effect of magnesium substitution in lithium nickel oxide an ab initio study. *J. Electrochem. Soc.* **151**, J91–J94 (2004). doi:10.1149/1.1809584

8. J. Graetz, C. C. Ahn, R. Yazami, B. Fultz, An electron energy-loss spectrometry study of charge compensation in $LiNi_{0.8}Co_{0.2}O_2$. *J. Phys. Chem. B* **107**, 2887–2891 (2003). doi:10.1021/jp026484y

9. S. Laha, S. Natarajan, J. Gopalakrishnan, E. Morán, R. Sáez-Puche, M. Á. Alario-Franco, A. J. Dos Santos-Garcia, J. C. Pérez-Flores, A. Kuhn, F. García-Alvarado, Oxygen-participated electrochemistry of new lithium-rich layered oxides Li_3MRuO_5 (M = Mn, Fe). *Phys. Chem. Chem. Phys.* **17**, 3749–3760 (2015). Medline doi:10.1039/C4CP05052E

10. H. Koga, L. Croguennec, M. Menetrier, P. Mannessiez, F. Weill, C. Delmas, S. Belin, Operando x-ray absorption study of the redox processes involved upon cycling of the Li-rich layered oxide $Li_{1.20}Mn_{0.54}Co_{0.13}Ni_{0.13}O_2$ in Li ion batteries. *J. Phys. Chem. C* **118**, 5700–5709 (2014). doi:10.1021/jp412197z

11. M. Oishi, C. Yogi, I. Watanabe, T. Ohta, Y. Orikasa, Y. Uchimoto, Z. Ogumi, Direct observation of reversible charge compensation by oxygen ion in Li-rich manganese layered oxide positive electrode material, $Li_{1.16}Ni_{0.15}Co_{0.19}Mn_{0.50}O_2$. *J. Power Sources* **276**, 89–94 (2015). doi:10.1016/j.jpowsour.2014.11.104

12. W.-S. Yoon, K.-B. Kim, M.-G. Kim, M.-K. Lee, H.-J. Shin, J.-M. Lee, J.-S. Lee, C.-H. Yo, Oxygen contribution on Li-ion intercalation-deintercalation in $LiCoO_2$ investigated by O K-edge and Co L-edge x-ray absorption spectroscopy. *J. Phys. Chem. B* **106**, 2526–2532 (2002). doi:10.1021/jp013735e

13. M. Sathiya, G. Rousse, K. Ramesha, C. P. Laisa, H. Vezin, M. T. Sougrati, M.-L. Doublet, D. Foix, D. Gonbeau, W. Walker, A. S. Prakash, M. Ben Hassine, L. Dupont, J.-M. Tarascon, Reversible anionic redox chemistry in high-capacity layered-oxide electrodes. *Nat. Mater.* **12**, 827–835 (2013). Medline doi:10.1038/nmat3699

14. M. Sathiya, A. M. Abakumov, D. Foix, G. Rousse, K. Ramesha, M. Saubanère, M. L. Doublet, H. Vezin, C. P. Laisa, A. S. Prakash, D. Gonbeau, G. VanTendeloo, J.-M. Tarascon, Origin of voltage decay in high-capacity layered oxide electrodes. *Nat. Mater.* **14**, 230–238 (2015). Medline doi:10.1038/nmat4137

15. M. Sathiya, K. Ramesha, G. Rousse, D. Foix, D. Gonbeau, A. S. Prakash, M. L. Doublet, K. Hemalatha, J.-M. Tarascon, High performance $Li_2Ru_{1-y}Mn_yO_3$ ($0.2 \leq y \leq 0.8$) cathode materials for rechargeable lithium-ion batteries: Their understanding. *Chem. Mater.* **25**, 1121–1131 (2013). doi:10.1021/cm400193m

16. E. McCalla, A. S. Prakash, E. Berg, M. Saubanère, A. M. Abakumov, D. Foix, B. Klobes, M.-T. Sougrati, G. Rousse, F. Lepoivre, S. Mariyappan, M.-L. Doublet, D. Gonbeau, P. Novak, G. Van Tendeloo, R. P. Hermann, J.-M. Tarascon, Reversible Li-intercalation through oxygen reactivity in Li-rich Li-Fe-Te oxide materials. *J. Electrochem. Soc.* **162**, A1341–A1351 (2015). doi:10.1149/2.0991507jes

17. J. Rouxel, Anion–cation redox competition and the formation of new compounds in highly covalent systems. *Chem. Eur. J.* **2**, 1053–1059 (1996). doi:10.1002/chem.19960020904

18. M. Sathiya, K. Ramesha, G. Rousse, D. Foix, D. Gonbeau, K. Guruprakash, A. S. Prakash, M. L. Doublet, J.-M. Tarascon, Li_4NiTeO_6 as a positive electrode for Li-ion batteries. *Chem. Commun.* **49**, 11376–11378 (2013). Medline doi:10.1039/c3cc46842a

19. E. McCalla, M.-T. Sougrati, G. Rousse, E. J. Berg, A. Abakumov, N. Recham, K. Ramesha, M. Sathiya, R. Dominko, G. Van Tendeloo, P. Novák, J.-M. Tarascon, Understanding the roles of anionic redox and oxygen release during electrochemical cycling of lithium-rich layered Li_4FeSbO_6. *J. Am. Chem. Soc.* **137**, 4804–4814 (2015). Medline doi:10.1021/jacs.5b01424

20. A. R. Armstrong, M. Holzapfel, P. Novák, C. S. Johnson, S.-H. Kang, M. M. Thackeray, P. G. Bruce, Demonstrating oxygen loss and associated structural reorganization in the lithium battery cathode $Li[Ni_{0.2}Li_{0.2}Mn_{0.6}]O_2$. *J. Am. Chem. Soc.* **128**, 8694–8698 (2006). Medline doi:10.1021/ja062027+

21. N. Yabuuchi, M. Takeuchi, M. Nakayama, H. Shiiba, M. Ogawa, K. Nakayama, T. Ohta, D. Endo, T. Ozaki, T. Inamasu, K. Sato, S. Komaba, High-capacity electrode materials for rechargeable lithium batteries: Li_3NbO_4-based system with cation-disordered rocksalt structure. *Proc. Natl. Acad. Sci. U.S.A.* **112**, 7650–7655 (2015). Medline doi:10.1073/pnas.1504901112

22. Materials and methods are available as supplementary materials on *Science* Online.

23. H. Kobayashi, M. Tabuchi, M. Shikano, H. Kageyama, R. Kanno, Structure, and magnetic and electrochemical properties of layered oxides, Li_2IrO_3. *J. Mater. Chem.* **13**, 957–962 (2003). doi:10.1039/b207282c

24. S. D. Findlay, N. Shibata, H. Sawada, E. Okunishi, Y. Kondo, Y. Ikuhara, Dynamics of annular bright field imaging in scanning transmission electron microscopy. *Ultramicroscopy* **110**, 903–923 (2010). Medline doi:10.1016/j.ultramic.2010.04.004

25. R. Ishikawa, E. Okunishi, H. Sawada, Y. Kondo, F. Hosokawa, E. Abe, Direct imaging of hydrogen-atom columns in a crystal by annular bright-field electron microscopy. *Nat. Mater.* **10**, 278–281 (2011). Medline doi:10.1038/nmat2957

26. L. Gu, D. Xiao, Y.-S. Hu, H. Li, Y. Ikuhara, Atomic-scale structure evolution in a quasi-equilibrated electrochemical process of electrode materials for rechargeable batteries. *Adv. Mater.* **27**, 2134–2149 (2015). Medline doi:10.1002/adma.201404620

27. D. Batuk, M. Batuk, A. M. Abakumov, J. Hadermann, Synergy between transmission electron microscopy and powder diffraction: Application to modulated structures. *Acta Crystallogr. B* **71**, 127–143 (2015). Medline

28. S. C. Yin, Y. H. Rho, I. Swainson, L. F. Nazar, X-ray/neutron diffraction and electrochemical studies of lithium de/re-intercalation in $Li_{1-x}Co_{1/3}Ni_{1/3}Mn_{1/3}O_2$ ($x = 0 \rightarrow 1$). *Chem. Mater.* **18**, 1901–1910 (2006). doi:10.1021/cm0511769

29. F. Grasset, C. Dussarrat, J. Darriet, Preparation, thermal stability and crystal structure of a new ruthenium(V) oxide containing peroxide ions: $Ba_5Ru_2O_9(O_2)$. Structural relationships to the hexagonal-type perovskite. *J. Mater. Chem.* **7**, 1911–1915 (1997). doi:10.1039/a701085k

30. M. Sathiya, J.-B. Leriche, E. Salager, D. Gourier, J.-M. Tarascon, H. Vezin, Electron paramagnetic resonance imaging for real-time monitoring of Li-ion batteries. *Nat. Commun.* **6**, 6276 (2015). Medline doi:10.1038/ncomms7276

31. J. Lee, A. Urban, X. Li, D. Su, G. Hautier, G. Ceder, Unlocking the potential of cation-disordered oxides for rechargeable lithium batteries. *Science* **343**, 519–522 (2014). Medline doi:10.1126/science.1246432

32. The FAULTS program is distributed within the FullProf Suite, available at www.ill.eu/sites/fullprof/index.html.

33. E. McCalla, A. Abakumov, G. Rousse, M. Reynaud, M. Sougrati, B. Budic, A. Mahdoud, R. Dominko, G. Van Tendeloo, R. P. Hermann, J.-M. Tarascon, Novel complex stacking of fully-ordered transition metal layers in Li_4FeSbO_6 materials. *Chem. Mater.* **27**, 1699–1708 (2015). doi:10.1021/cm504500a

34. M. T. Sougrati, J. Fullenwarth, A. Debenedetti, B. Fraisse, J. C. Jumas, L. Monconduit, TiSnSb a new efficient negative electrode for Li-ion batteries: Mechanism investigations by operando-XRD and Mössbauer techniques. *J. Mater. Chem.* **21**, 10069–10076 (2011). doi:10.1039/c1jm10710k

35. J.-C. Jumas, L. Stievano, M. T. Sougrati, J. Fullenwarth, B. Fraisse, J.-B. Leriche, “Analyse des caracteristiques d’un matériau d’électrode d'une cellule électrochimique.” Patent WO2014033402 A1 (2013).

36. E. J. Berg, P. Novák, in Annual Report 2012: Electrochemistry Laboratory (Paul Scherrer Institut, 2012), p. 47, www.psi.ch/lec/AnnualReportsUebersichtsTabelle/ECL-Annual-Report_2012.pdf.

37. G. Kresse, J. Hafner, Ab initio molecular dynamics for liquid metals. *Phys. Rev. B* **47**, 558–561 (1993). Medline doi:10.1103/PhysRevB.47.558

38. G. Kresse, J. Furthmuller, Efficiency of ab-initio total energy calculations for metals and semiconductors using a plane-wave basis set. *Comput. Mater. Sci.* **6**, 15–50 (1996). doi:10.1016/0927-0256(96)00008-0

39. J. P. Perdew, K. Burke, M. Ernzerhof, Generalized gradient approximation made simple. *Phys. Rev. Lett.* **77**, 3865–3868 (1996). Medline doi:10.1103/PhysRevLett.77.3865

40. S. L. Dudarev, G. A. Botton, S. Y. Savrasov, C. J. Humphreys, A. P. Sutton, Electron-energy-loss spectra and the structural stability of nickel oxide: An LSDA+U study. *Phys. Rev. B* **57**, 1505–1509 (1998). doi:10.1103/PhysRevB.57.1505

41. P. E. Blöchl, Projector augmented-wave method. *Phys. Rev. B* **50**, 17953–17979 (1994). Medline doi:10.1103/PhysRevB.50.17953

42. G. Kresse, D. Joubert, From ultrasoft pseudopotentials to the projector augmented-wave method. *Phys. Rev. B* **59**, 1758–1775 (1999). doi:10.1103/PhysRevB.59.1758

43. C. T. Koch, thesis, Arizona State University (2002).